Electrochimica Acta 83 (2012) 410–419

Contents lists available at SciVerse ScienceDirect

Electrochimica Acta

journal homepage: www.elsevier.com/locate/electacta

Electrochemical reduction of hydrogen peroxide on SIMFUEL (UO_2) in acidic pH conditions

Mayuri Razdan, David S. Hall[1], Peter G. Keech[2], David W. Shoesmith*

Department of Chemistry, Western University, 1151 Richmond Road, London, ON, Canada N6A 5B7

ARTICLE INFO

Article history:
Received 22 March 2012
Received in revised form 16 May 2012
Accepted 30 May 2012
Available online xxx

Keywords:
Uranium dioxide
Hydrogen peroxide
Corrosion
Acidic pH
X-ray photoelectron spectroscopy (XPS)

ABSTRACT

The present study aims to investigate the electrochemical reduction of a range of H_2O_2 concentrations on a 1.5 at.% SIMFUEL rotating disk electrode over the pH range 1–4. The peroxide reduction mechanism is determined to occur either on a U^V-containing surface layer of composition $U^{IV}_{1-2x}U^V_{2x}O_{2+x}$ or on an adsorbed U^V-containing surface intermediate depending on the surface composition which is determined by solution pH and H_2O_2 concentration. The $U^{IV}_{1-2x}U^V_{2x}O_{2+x}$ catalytic surface lattice layer, if formed, is stable and rotation disk studies have demonstrated that H_2O_2 reduction on this surface achieves the diffusion-controlled limit at sufficiently negative overpotentials. However, the adsorbed U^V-containing surface intermediate is unstable and can be destroyed by electrochemical reduction to its original state, i.e. UO_2, or by chemical oxidation to U^{VI} prior to dissolution as UO_2^{2+}.

The instability of this surface intermediate limits its availability which prevents significant H_2O_2 reduction and yields currents below the diffusion-controlled limit. The occurrence of both reduction mechanisms demonstrates the influence of locally established surface compositions and the switch from one to the other appears to be controlled by surface diffusion conditions and the bulk pH and H_2O_2 concentrations.

1. Introduction

While nuclear power represents a clean and safe form of energy generation it comes with the responsibility of managing the radioactive fuel waste. Internationally, deep geologic disposal is the primary option for long term nuclear waste management. In the Canadian approach, used nuclear fuel bundles would be sealed in corrosion resistant containers, emplaced in a vault excavated deep underground in a stable geologic formation [1,2]. Safety assessments conservatively assume that some containers will be emplaced with undetected defects which could allow groundwater to contact the fuel waste form and initiate its corrosion/dissolution.

Assuming that the containers remain unbreached until the β- and γ-radiation fields have decayed to insignificant levels (a process which will take a few hundred years [3]), then the primary source of oxidants will be the α-radiolysis of water,

$$2H_2O \xrightarrow{\alpha} H_2O_2 + H_2 \quad (1)$$

Among the several oxidants produced, H_2O_2 is considered the most likely to cause fuel corrosion, and the potential effects of this oxidant have been studied in detail [3–20]. H_2O_2 reduction on UO_2 surfaces occurs via a coupled chemical–electrochemical process in which U^{IV}–U^V donor–acceptor sites are first chemically created on the UO_2 surface by H_2O_2 and subsequently destroyed electrochemically,

$$2U^{IV} + H_2O_2 \rightarrow 2U^V + 2OH^- \quad (2)$$

$$2U^V + 2e^- \rightarrow 2U^{IV} \quad (3)$$

Under natural corrosion conditions, reaction (3) is coupled to the oxidation and dissolution of UO_2 as UO_2^{2+}

$$UO_2 \rightarrow UO_2^{2+} + 2e^- \quad (4)$$

although it could also lead to the oxidation of H_2O_2

$$H_2O_2 \rightarrow O_2 + 2H^+ + 2e^- \quad (5)$$

resulting in its overall decomposition.

Based on an original suggestion by Nicol and Needes [21], Keech et al. [12] proposed that, for the low pH region (pH <3), H_2O_2 reduction is catalyzed by a surface adsorbed U^V species ($U^VO_2OH_{ads}$) created by the chemical reaction (2). In less acidic solutions (pH ~5–9) the U^V state is created within the UO_2 matrix by incorporation of O^{2-} anions at interstitial sites creating a $U^{IV}_{1-2x}U^V_{2x}O_{2+x}$ surface layer. This layer is considerably more stable than the

* Corresponding author. Tel.: +1 519 661 2111x86366.
E-mail address: dwshoesm@uwo.ca (D.W. Shoesmith).
[1] Present address: Department of Chemistry, University of Ottawa, 10 Marie Curie, Ottawa, ON, Canada K1N 6N5.
[2] Present address: Nuclear Waste Management Organization (NWMO), Toronto, ON, Canada M4T 2S3.

0013-4686/$ – see front matter © 2012 Elsevier Ltd. All rights reserved.
http://dx.doi.org/10.1016/j.electacta.2012.05.163

adsorbed state formed in acidic solutions and can sustain H_2O_2 reduction at the diffusion-controlled limit [6,12].

Further oxidation of this surface layer can lead to the formation of a corrosion product deposit ($UO_3{\cdot}yH_2O$), but for pH <6 this phase undergoes chemical dissolution (as UO_2^{2+}) and the UO_2 dissolution rate increases considerably [22]. The literature suggests that the presence of H_2O_2 at sufficient concentrations can also lead to the formation of uranyl peroxides, such as studtite ($UO_4{\cdot}4H_2O$), which can be the dominant secondary phase rather than schoepite ($UO_3{\cdot}2H_2O$) [23–29]. Calorimetric calculations [24] indicate that studtite can form in the presence of $[H_2O_2]$ as low as 10^{-14} mol L^{-1}, and it is reported to inhibit H_2O_2 reduction on fuel surfaces leading to steady-state uranium concentrations during leaching experiments [30]. However, HCO_3^-/CO_3^{2-} can influence the stability of these phases by complexing UO_2^{2+} [22], and Hanson has reported their solubility in acidic solutions [31]. In addition, these peroxy hydrates are reported to be unstable in the presence of ionizing radiation $\sim 10^6$ Gy (total absorbed dose) which leads to their partial amorphization and decomposition [32].

Although neutral to slightly alkaline conditions (pH 6–9.5) are expected to prevail under repository conditions, the possibility of producing acidic locations by UO_2^{2+} hydrolysis

$$nUO_2^{2+} + yH_2O \rightarrow (UO_2)_n(OH)_y^{(2n-y)+} + yH^+ \quad (6)$$

within corrosion product deposits and flaws in the fuel surface has been considered [10–15]. While unlikely, such a possibility is difficult to rule out on a spent fuel surface which will contain noble metal particles able to enforce the separation of anodes and cathodes.

With this possibility of local acidification in mind the electrochemical reduction of H_2O_2 has been studied over the pH range 1–9 [12]. While this study identified a change in mechanism with pH, the details remained obscure. In the study presented here a wider range of H_2O_2 concentrations have been studied over a narrower range of pH (1–4). The primary goal of the study is to identify the details of this change in mechanism with pH and how it is influenced by, or dictates, the composition of the UO_2 surface.

2. Experimental

2.1. Electrode material

Experiments were performed on a simulated nuclear fuel (SIMFUEL). SIMFUEL is a chemical analog of spent nuclear fuel fabricated by Atomic Energy of Canada Limited (Chalk River, Ont., Canada). The pellets are produced by doping the UO_2 matrix with a series of stable elements (Ba, Ce, La, Mo, Sr, Y, Rh, Pd, Ru, Nd, Zr) in the proportions required to simulate fuels of different in-reactor burn-up [33]. In this case the matrix was doped to simulate a burn-up of 1.5 at.% [33]. Doping leads to the substitution of trivalent rare-earth species for U^{IV} atoms in the fluorite lattice and the creation of a corresponding number of U^V species to maintain the charge balance. The noble metal dopants (Pd, Mo, Ru, Rh) separate as metallic particles uniformly distributed in the UO_2 matrix as spherical precipitates [33]. The electrodes were approximately 2 mm thick and 1.2 cm in diameter and were cut from a SIMFUEL pellet using a previously published procedure [34].

2.2. Electrochemical cell and equipment

All experiments were carried out in a standard three-electrode, three-compartment cell. The cell compartments were separated by glass frits to minimize contamination of the working electrode compartment. The working electrode was screwed on to the shaft of a Pine Instruments model AFASR analytical rotator and the rotation rates were varied from 5 to 33 Hz. All potentials were measured and are quoted against a saturated calomel reference electrode (SCE, Fischer Scientific). The counter electrode was a $\sim 6\,cm^2$ Pt sheet spot-welded to a Pt wire (99.9% purity, Alfa Aesar). The cell was housed in a grounded Faraday cage to minimize external sources of noise. A Solartron model 1287 potentiostat was used to record current responses as a function of applied potential and Corrware™, version 3.0, software was used to control the instrument and analyze the data. The current interrupt method (IR) was employed to compensate for potential drop due to the electrode and solution resistances.

2.3. Electrode polishing and solution preparation

Electrodes were prepared by polishing on wet 1200 SiC paper and rinsed with distilled deionized water. Subsequently, they were electrochemically cleaned at two different potentials, −1.5 V and −1.2 V for 5 min each (vs. SCE). This procedure removed any air formed oxides or organic contaminants. X-ray photoelectron spectroscopy (XPS) was used to investigate the chemical composition of the fuel surface after electrochemical measurements. On extraction from the cell, the electrode surface was immediately rinsed with Millipore water and air dried before loading into the XPS vacuum chamber.

Solutions used were prepared with distilled deionized water (resistivity (ρ) = 18.2 MΩ cm) purified using a Millipore Milli-Q-plus unit to remove organic and inorganic impurities. All experiments were performed in a 0.1 mol L^{-1} NaCl (Caledon, >99%) solution purged with Ar gas (Praxair). The solution pH was adjusted to the desired value using a reagent grade HCl solution, and monitored with an Orion model 720A pH meter. Hydrogen peroxide (Fisher Scientific, 3% w/v) was added to the electrochemical cell before the start of an experiment.

2.4. UV/vis spectrophotometry

The H_2O_2 concentration in the cell was determined by ultra-violet/visible spectrophotometry. All spectrophotometric measurements were performed using a BioLogic Science Instruments MOS 450 diode array UV/vis spectrophotometer. H_2O_2 concentrations were determined using the Ghormley tri-iodide method in which ammonium molybdate is used to catalyze the oxidation of I^- to I_3^- by H_2O_2. The maximum absorption of I_3^- was taken to occur at 350 nm with a molar extinction coefficient of 25,500 mol L^{-1} cm^{-1} [35,36]. The detection limit for H_2O_2 was 3×10^{-6} mol L^{-1}.

2.5. Scanning electron microscopy (SEM)

SEM micrographs were obtained using a Hitachi S-4500 Field emission scanning electron microscope. Immediately following experimentation, samples were rinsed with Millipore water and placed into the microscope. During image collection, the electron beam potential was maintained at 10.0 kV and the working distance was 10 mm.

2.6. X-ray photoelectron spectroscopy (XPS)

XPS analyses were performed on a Kratos Axis NOVA spectrometer. Spectra were collected using Al K_α-monochromatic radiation (15 mA, 14 kV) to bombard the surface with high energy monochromatic X-rays ($h\nu$ = 1486.6 eV). The instrument work function was set to give a binding energy (BE) of 83.96 eV for the Au $4f_{7/2}$ line for metallic gold and the spectrometer dispersion was adjusted to give a BE of 932.62 eV for the Cu $2p_{3/2}$ line of metallic copper. The instrument charge neutralizer was used on all specimens. Survey

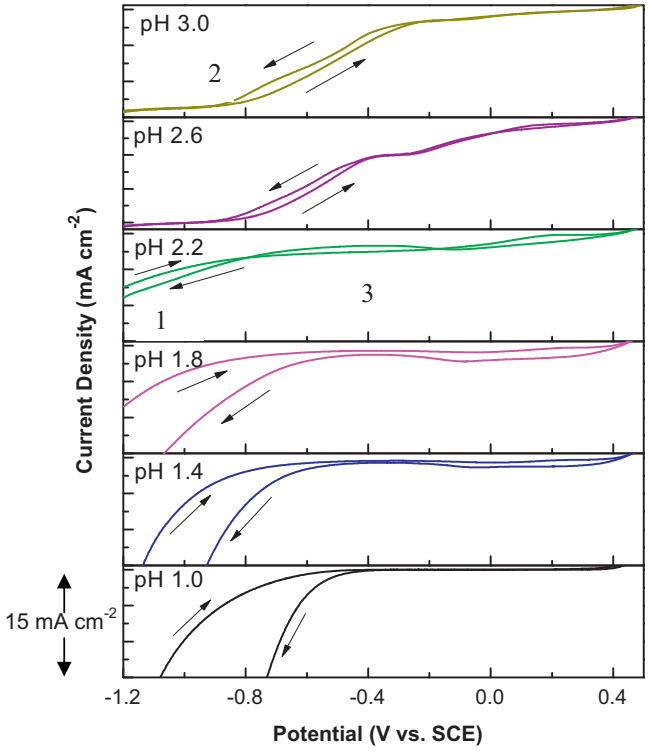

Fig. 1. Voltammograms recorded on a 1.5 at.% SIMFUEL at 10 mV s^{-1} at an electrode rotation rate of 16.7 Hz in 0.1 mol L^{-1} NaCl containing 5×10^{-3} mol L^{-1} H_2O_2 at different pH values. The scans are offset by 15 mA cm^{-2}.

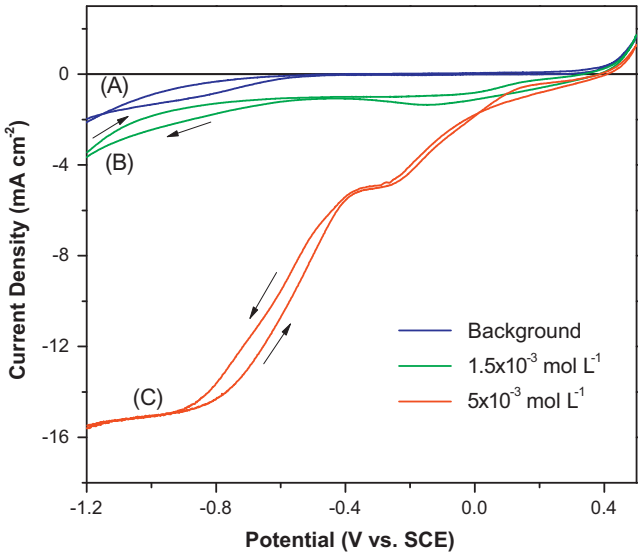

Fig. 2. Voltammograms recorded on a 1.5 at.% SIMFUEL at 10 mV s^{-1} at an electrode rotation rate of 16.7 Hz in 0.1 mol L^{-1} NaCl at pH 2.6 containing H_2O_2: (A) 0 mol L^{-1}; (B) 1.5×10^{-3} mol L^{-1} and (C) 5×10^{-3} mol L^{-1}. The arrows indicate scan direction.

spectra were recorded for the energy range 0–1100 eV with an analysis area of ~300 × 700 microns at a pass energy of 160 eV, and high resolution spectra for the U 4f, O 1s, C 1s and the U 5f valence band regions were collected with a pass energy of 20 eV. The carbon 1s line at 285 eV was used as a standard, when necessary, to correct for surface charging. Spectra were analyzed using CasaXPS software (version 2.3.14).

In many previous studies, researchers have opted to deconvolute the U $4f_{7/2}$ peak to avoid the complications due to overlap of the U $5f_{7/2}$ peak with a shake-up band associated with the U $4f_{7/2}$ satellite peak [34,37–39]. In this study, we have fitted both the two spin-orbit split peaks and the associated satellite structures following the procedure and recommendations of Schindler et al. [40] and Ilton et al. [41,42]. As discussed recently, there are advantages and disadvantages to both procedures consistent with the observations of Ilton et al. [43]: a 10–15% higher U^{VI} content is observed when ignoring the satellite structures in the fitting procedure. Acknowledging these ambiguities we have resolved the 4f spectrum into contributions from U^{IV}, U^{V}, and U^{VI}. Table 1 summarizes the fitting parameters used, where the separation between the U $4f_{7/2}$ and U $4f_{5/2}$ and between the deconvoluted peaks under the main 4f peak are adopted from the literature [40–43]. Following a Shirley background correction, Gaussian–Lorentzian peak shapes were used: 50% Lorentzian for the main $4f_{7/2}$ and $4f_{5/2}$ peaks and 30% Lorentzian for the satellite peaks.

3. Results and discussion

3.1. Voltammetry

A series of voltammograms recorded in H_2O_2-containing solutions with various pH values ranging from 1 to 3 are shown in Fig. 1. The various stages of reduction are numbered and the features present are consistent with previous observations [12]. The reduction current observed in region 1 (at the most negative potentials) can be attributed to H^+ reduction catalyzed on noble metal particles in the SIMFUEL matrix [44,45] and therefore, as the pH is decreased, the current density increases. However, in very acidic conditions the H^+ reduction current is large and the hysteresis observed between the forward and reverse scans obscures the current for H_2O_2 reduction. The enhanced H^+ reduction current observed on the reverse scan at pH 1.0, 1.4 and 1.8 indicates a sensitization of the UO_2 surface by the formation (forward scan) and reduction (reverse scan) of oxidized species. At pH 3, the reduction current observed in region 2 is a characteristic of H_2O_2 reduction on a $U^{IV}{}_{1-2x}U^{V}{}_{2x}O_{2+x}$ surface layer formed by the injection of O^{2-} anions into the UO_2 lattice accompanied by the creation of a U^V surface species, reaction (2). The kinetics of H_2O_2 reduction on such a layer has been investigated in detail [6–9]. Rotating disk studies have shown that H_2O_2 reduction on this surface can achieve mass transport control at sufficiently negative potentials (≤ -0.8 V vs. SCE) [7]. However, at pH 3 the formation of such a layer is unexpected, since it should be thermodynamically unstable in solutions with a pH <5 [46]. Its presence would be consistent with the elevation of the pH at the electrode surface by OH^- production, reaction (2).

A separate H_2O_2 reduction pathway was observed in region 3 for pH ≤2.60, Fig. 1, attributed to H_2O_2 reduction catalyzed by the adsorbed U^V surface species $(U^VO_2OH)_{ads}$, formed by surface coordination with OH^- [12]. It was claimed that this intermediate is unstable to electrochemical reduction, which prevents the H_2O_2 reduction current from increasing to the diffusion-controlled value. At pH 2.6, both reduction processes occur suggesting localized surface regions of low and high pH. As will be shown below, the surface of the electrode is rough allowing the convective/diffusive conditions to vary with surface location.

In support of this argument, Fig. 2 shows CVs recorded with and without H_2O_2 at pH 2.6. The low background current (A) shows that any contribution from H^+ reduction is very small at this pH and confined to very negative potentials. The CV recorded at the lower $[H_2O_2]$ shows only the current associated with region 3 while at the higher $[H_2O_2]$ current was observed in both regions 2 and 3. The observation of a current in region 2 only at the higher $[H_2O_2]$ is consistent with the need for a high $[OH^-]$ to stabilize the catalytic $U^{IV}{}_{1-2x}U^{V}{}_{2x}O_{2+x}$ layer.

Table 1
Peak binding energies used for U ($4f_{7/2}$) and satellite peak positions associated with U ($4f_{5/2}$).

	U $4f_{7/2}$ (eV)	U $4f_{5/2}$ (eV)		References
UO_2 main peaks	379.9–381.0	390.8–391.9		
Main peak FWHM (eV)	1.55			
	1.38			[51]
	1.65			[40]
Separation between $U_{7/2}$ and $U_{5/2}$ peaks (eV)	10.9			
	10.9			[40]
Peak separation between primary peaks (eV)	U(IV)–U(V)	U(V)–U(VI)	U(IV)–U(VI)	
	0.85	0.85	1.7	
	0.8	1.0	1.8	[51]
	0.9	0.8	1.7	[40]
Separation between main peak and satellite (eV)	$U(IV)_{5/2}$	$U(V)_{5/2}$	$U(VI)_{5/2}$	
	6.3–7.0	8.1	4.0, 10.0	
	6.3	8	4.0, 10.0	[42]
	6.6	8.1	4.0, 10.0	[40]

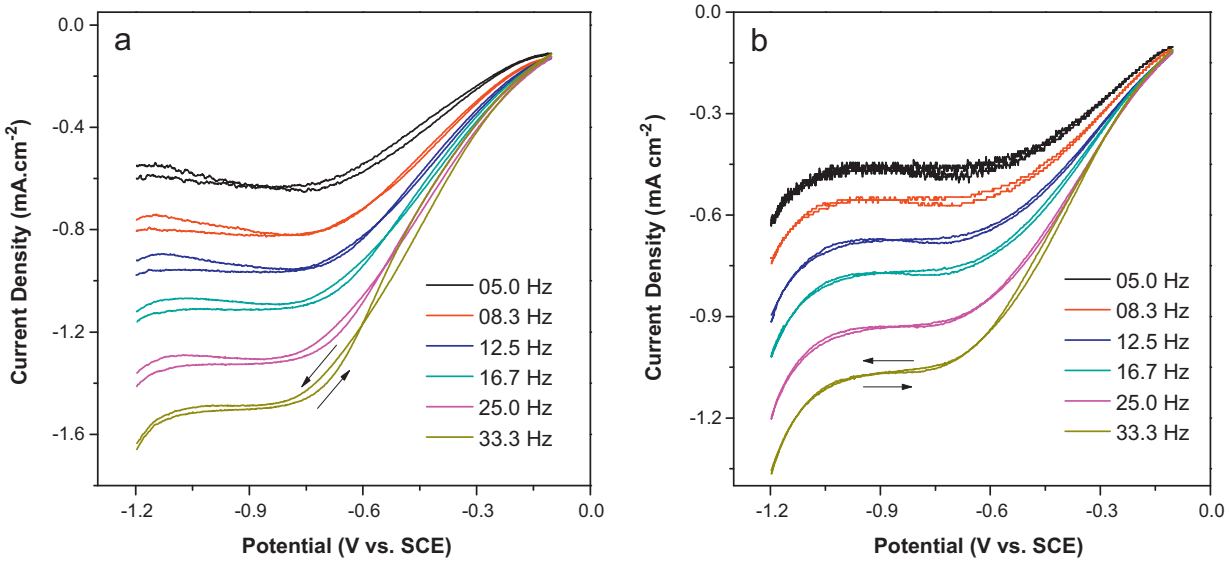

Fig. 3. Voltammograms recorded on a 1.5 at.% SIMFUEL RDE at 10 mV s^{-1} in Ar-purged 0.1 mol L^{-1} NaCl solution at pH 4 in solutions containing H_2O_2 (a) 6.5×10^{-4} mol L^{-1} and (b) 4.9×10^{-4} mol L^{-1}. The currents have been corrected for the background current recorded in the absence of H_2O_2. The arrows indicate scan direction.

Fig. 3(a) and (b) shows background-corrected H_2O_2 reduction curves recorded at pH 4 for two slightly different $[H_2O_2]$ as a function of electrode rotation rate. At both concentrations, a well-developed, rotation rate-dependent, current density plateau is observed at high overpotentials suggesting H_2O_2 reduction is diffusion-controlled when the local pH becomes sufficiently high to stabilize a $U^{IV}_{1-2x}U^{V}_{2x}O_{2+x}$ surface layer. However, comparison of the plateau currents to the theoretical diffusion-limiting currents, calculated using the Levich equation [47] and a diffusion coefficient adopted from Goldik et al. [7], show deviations from the limiting current values which depend both on electrode rotation rate and $[H_2O_2]$ (Fig. 4(a) and (b)). As can be seen in Fig. 5, which plots the ratio of the measured currents to the theoretical diffusion-limited values, diffusion control is only achieved at low electrode rotation rates at both concentrations when the flux of OH^- away from, or H^+ to, the electrode surface will be at its lowest and the surface pH at its highest. Additionally, even though the difference in $[H_2O_2]$ in the two experiments is small, the deviation from diffusion control, indicating the onset of a kinetically-limited process, commences at a lower rotation rate and is more significant at the lower $[H_2O_2]$ (Fig. 4(b)) when the surface disturbance of pH by H_2O_2 reduction will be less marked.

A similar set of background-corrected H_2O_2 reduction curves and a Levich plot, recorded at pH 3 ($[H_2O_2] = 8.3 \times 10^{-4}$ mol L^{-1}) as a function of electrode rotation rate, are shown in Fig. 6. No diffusion-controlled reduction process is observed in the −0.75 V to −1.1 V range (Fig. 6(a)) and the H_2O_2 reduction current only increases toward the diffusion-controlled limit at very negative potentials. Fig. 6(b) confirms this behavior, the deviation from theoretical diffusion-limiting current values indicating H_2O_2 reduction is kinetically inhibited. Although the currents are corrected for the contribution from H^+ reduction they will be influenced by the local pH increase associated with this reaction occurring in an unbuffered solution (Fig. 6(a)). Thus, the large, but potential-delayed H_2O_2 reduction currents can be attributed to this pH increase and the eventual stabilization of the $U^{IV}_{1-2x}U^{V}O_{2+x}$ layer. The ratio of the measured (at −0.8 V) to the diffusion-limited current for this $[H_2O_2]$ is included in Fig. 5, and it is clear that only a limited current for H_2O_2 reduction is observed and that it is only marginally-dependent on electrode rotation rate. These observations suggest the H_2O_2 reduction current is kinetically rather than diffusion-controlled at this pH and $[H_2O_2]$. Comparison of the three sets of data, Fig. 5, indicates a transition from diffusion control to kinetic control occurs as the $[H_2O_2]/[H^+]$ decreases.

At an intermediate pH of 3.5 and with only slightly different $[H_2O_2]$ a very distinct hysteresis occurs between the forward and reverse scans and both types of behavior are observed, Fig. 7. Comparison of Fig. 7(a) and (b) shows the transition between the two reduction mechanisms depends on pH, $[H_2O_2]$, and the potential on the forward and reverse voltammetric scans. On the forward scan

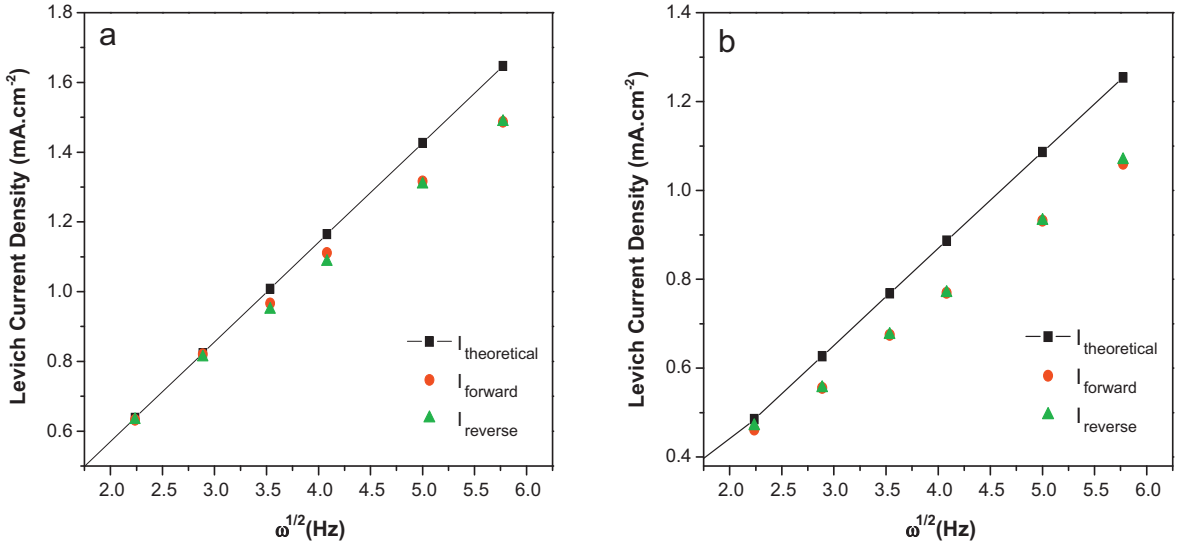

Fig. 4. Levich plots for H_2O_2 reduction currents recorded on a 1.5 at.% SIMFUEL RDE in Ar-purged 0.1 mol L^{-1} NaCl solution at pH 4 in solutions containing H_2O_2 (a) 6.5×10^{-4} mol L^{-1} and (b) 4.9×10^{-4} mol L^{-1}. The currents have been corrected for the background current recorded in the absence of H_2O_2.

from −1.2 V, alkaline conditions are initially established at the electrode surface due to H^+ and H_2O_2 reduction. Under these conditions the catalytic surface layer ($U^{IV}_{1-2x}U^{V}_{2x}O_{2+x}$) is formed and the H_2O_2 reduction current approaches the diffusion-controlled limit. As the potential becomes more positive, this catalytic layer is destabilized due to the decreased rate of OH^- production and the formation of $(U^{V}O_2OH)_{ads}$ occurs, at least on some areas of the electrode surface. As will be shown below, the surface is rough and hence the convective/diffusive conditions will vary somewhat from location to location on the fuel surface. Consequently, the pH will also change slightly from location to location leading to some non-uniformity in the transition between processes. The onset of this transition in surface state accounts for the kink (~−0.4 V) in H_2O_2 reduction current at the higher [H_2O_2], Fig. 7(a), and the very rapid drop in this current ($E < -0.7$ V) at the slightly lower [H_2O_2], Fig. 7(b). This is clearly demonstrated in Fig. 8(a) and (b) which shows scans to various anodic limits for two different electrode rotation rates in the solution containing the higher [H_2O_2]. The observation of hysteresis at the high rotation rate only, confirms that its development is very dependent on surface pH.

As demonstrated previously [10,12], this U^V intermediate becomes unstable at potentials more positive than ~−0.2 V and is electrochemically oxidized and subsequently dissolved.

$$(U^{V}O_2OH)_{ads} + H_2O \rightarrow (U^{VI}O_2(OH)_2)_{ads} + H^+ + e^- \quad (7)$$

$$(U^{VI}O_2(OH)_2)_{ads} + 2H^+ \rightarrow UO_2^{2+} + 2H_2O \quad (8)$$

On the reverse scan from an anodic limit of −0.1 V the cathodic current increases slightly for $E \leq -0.2$ V; i.e., when the potential becomes too negative for the electrochemical oxidation reaction (7). Subsequently, a low potential-independent cathodic reduction current is stabilized over a potential range which depends on [H_2O_2] and electrode rotation rate. At the higher [H_2O_2], Fig. 7(a), once a sufficiently negative potential is achieved, the H_2O_2 reduction current rises steeply toward the diffusion limit for all electrode rotation rates. This rise indicates that sufficiently alkaline conditions are established at the electrode surface to stabilize a $U^{IV}_{1-2x}U^{V}_{2x}O_{2+x}$ layer allowing the H_2O_2 reduction current to rise toward the diffusion-controlled limit.

While a current close to the diffusion-controlled value is eventually achieved at all electrode rotation rates, the increase toward this value commences at lower potentials for the lower electrode rotation rate; i.e., the lower the diffusive flux of OH^- from, or H^+ to, the electrode surface the more rapidly a high pH is established at the electrode surface. That this is the case is more clearly illustrated at the lower [H_2O_2], Fig. 7(b), when the local pH will be more readily neutralized by OH^-/H^+ transport. The potential at which the H_2O_2 reduction current begins to rise is more obviously rotation rate dependent. Additionally, considerably more negative potentials are required for the current to approach the diffusion-controlled limit. For the higher electrode rotation rates, the H_2O_2 reduction current does not approach the diffusion limit within the range of potentials investigated.

That the composition of the electrode surface is dictated by a balance between the rate of OH^- production by H_2O_2 reduction and the flux of OH^-/H^+ from/to the electrode surface is confirmed by the plot of the ratio of the measured background-corrected currents to theoretically calculated diffusion-limiting currents in Fig. 9. The H_2O_2 reduction current only approaches the diffusion limit when

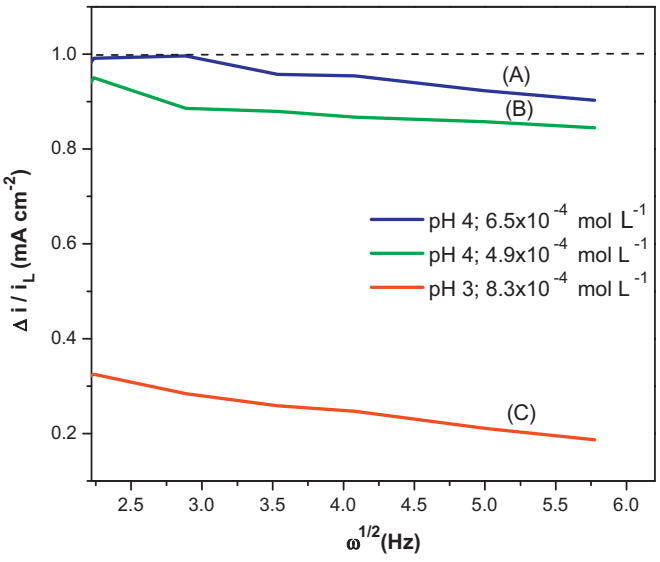

Fig. 5. The ratio of the background corrected currents (Δi) to the theoretical diffusion limiting current (i_L) recorded as a function of electrode rotation rate at −0.8 V in 0.1 mol L^{-1} NaCl solutions for (a) pH 4; [H_2O_2] = 6.5×10^{-4} mol L^{-1} (b) pH 4; [H_2O_2] = 4.9×10^{-4} mol L^{-1} and (c) pH 3; [H_2O_2] = 8.3×10^{-4} mol L^{-1}.

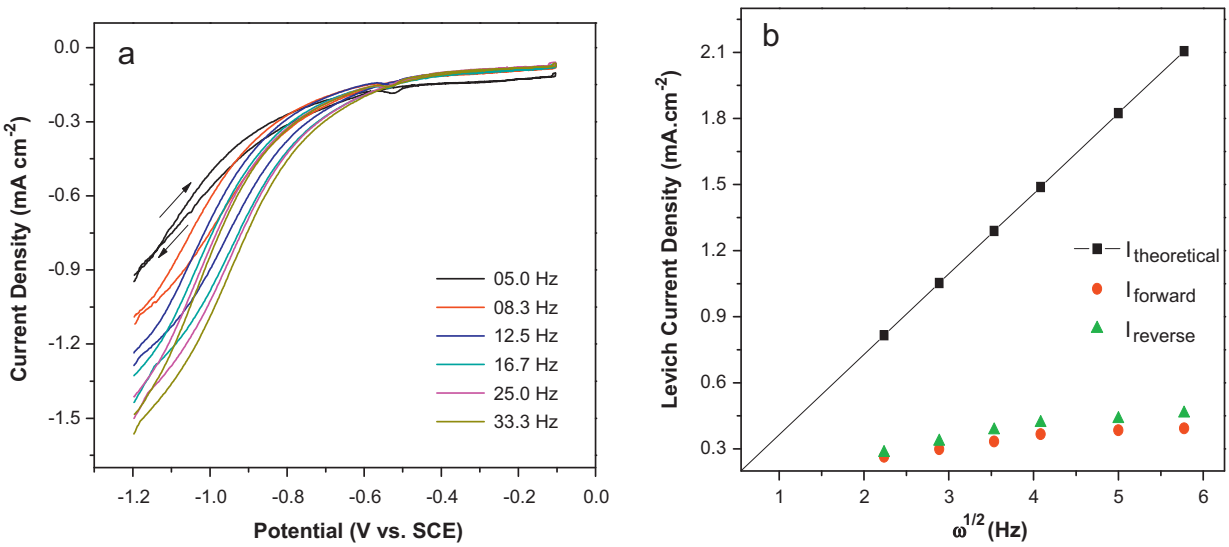

Fig. 6. (a) Voltammograms and (b) Levich plot for H_2O_2 reduction current recorded on a 1.5 at.% SIMFUEL RDE in Ar-purged 0.1 mol L^{-1} NaCl solutions at pH 3 containing 8.3×10^{-4} mol L^{-1} H_2O_2. The currents have been corrected for the background current recorded in the absence of H_2O_2.The arrows indicate scan direction.

its concentration is sufficiently high that the production of OH^- cannot be neutralized at that pH.

3.2. XPS analyses

The evidence presented above clearly demonstrates two distinct pathways for the cathodic reduction of H_2O_2 depending on the pH at the electrode surface. The kinetics and mechanism of this reaction on the $U^{IV}_{1-2x}U^{V}_{2x}O_{2+x}$ surface stabilized at pH ≥5 have been studied in detail [6–9] but only a preliminary mechanism developed for the mechanism in more acidic solutions [12]. The constant current for H_2O_2 reduction observed over a wide potential range, Figs. 2 and 6, is consistent with the presence of the proposed $(U^{V}O_2OH)_{ads}$ surface intermediate which can either be further oxidized to soluble UO_2^{2+} via reactions (7) and (8) or reduced back to the substrate UO_2 via reaction (9):

$$(U^{V}O_2OH)_{ads} + e^- \rightarrow UO_2 + OH^- \quad (9)$$

To investigate this mechanism in acidic solutions in more detail, potentiostatic experiments were performed at −0.2 V in 0.1 mol L^{-1} NaCl (pH 3.5) solution with and without added H_2O_2. Theelectrode was subsequently analyzed by XPS to determine the relative abundances of the three oxidation states of U (U^{IV}, U^{V}, U^{VI}) in the electrode surface.

Fig. 10 shows the background-corrected steady-state currents recorded over the $[H_2O_2]$ range from 0 to 8×10^{-3} mol L^{-1}. Steady-state was achieved in a few minutes at all concentrations. The dependence of the current on $[H_2O_2]$ confirms that the reduction current is due to H_2O_2 reduction. The current measured in the absence of H_2O_2 is insignificant suggesting only minor anodic oxidation and dissolution of the electrode surface.

Fig. 11 shows the high resolution XPS spectra recorded after potentiostatic oxidation in the absence and presence of H_2O_2. In the absence of H_2O_2, U^{IV} is the dominant oxidation state present in the electrode surface as clearly demonstrated by the location of the satellite peak at a binding energy of 7.0 eV higher than the U

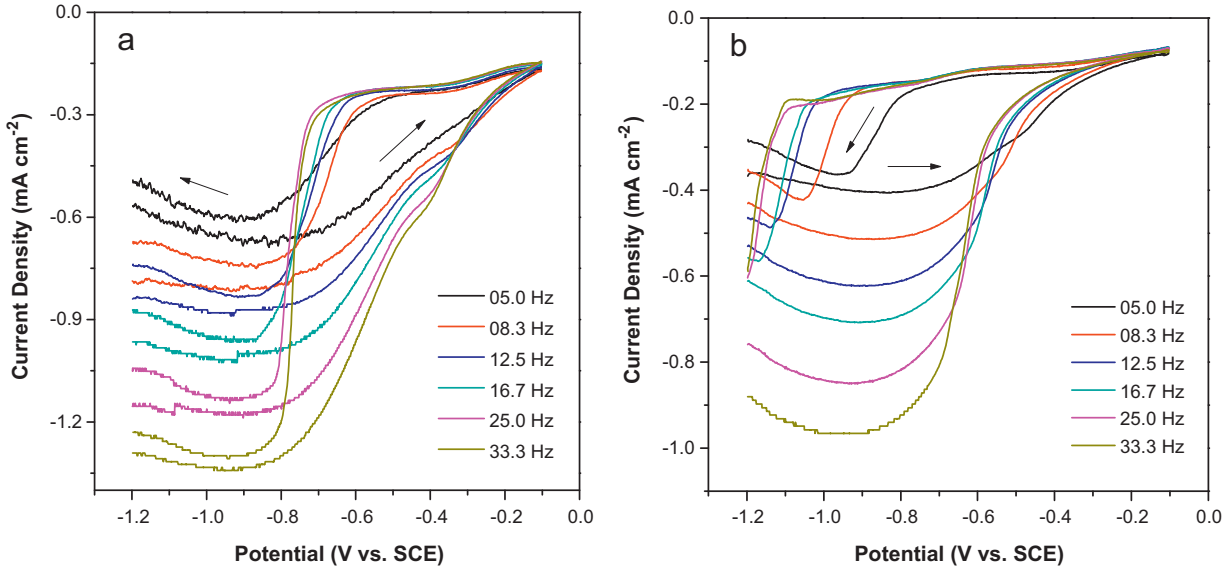

Fig. 7. Voltammograms for H_2O_2 reduction currents recorded on a 1.5 at.% SIMFUEL RDE in Ar-purged 0.1 M NaCl solutions at pH 3.5 containing H_2O_2 (a) 7.7×10^{-4} mol L^{-1} and (b) 4.4×10^{-4} mol L^{-1}. The currents have been corrected for the background current recorded in the absence of H_2O_2. The arrows indicate scan direction.

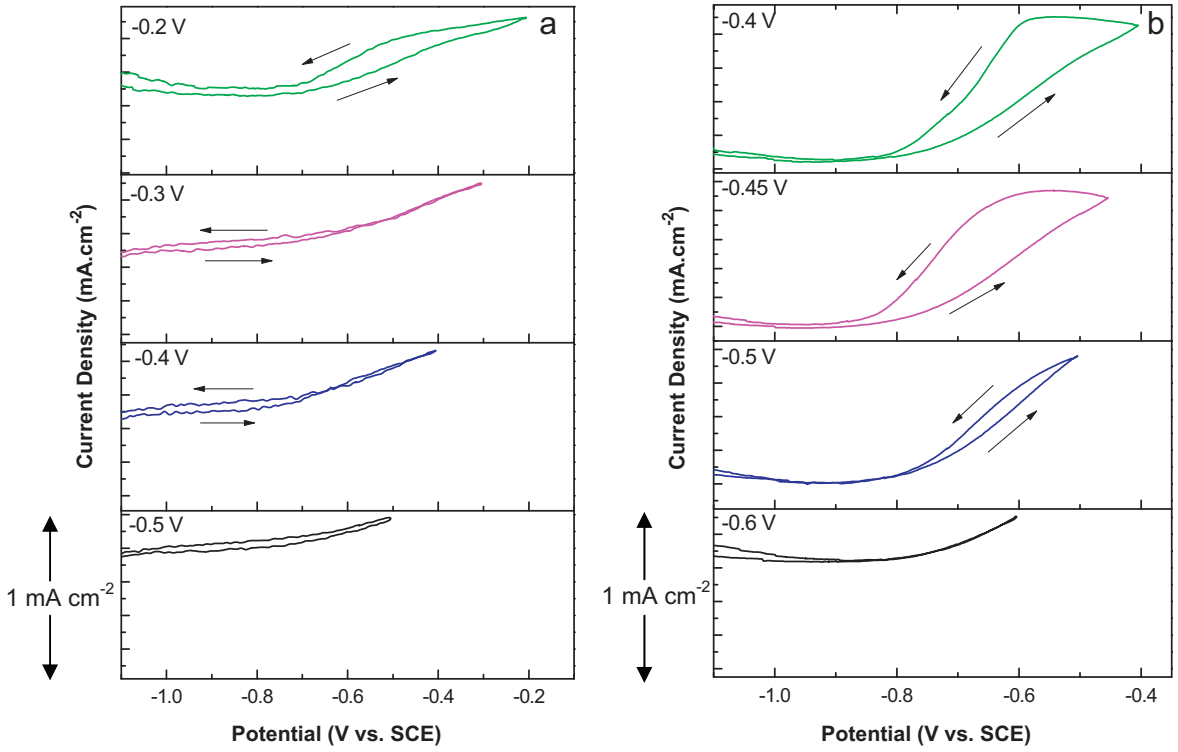

Fig. 8. Voltammograms to various anodic potential limits for H_2O_2 reduction currents recorded on a 1.5 at.% SIMFUEL RDE in Ar-purged 0.1 M NaCl at pH 3.5 containing 7.7×10^{-4} mol L^{-1} H_2O_2: (a) 5.0 Hz and (b) 25 Hz. The currents have been corrected for the background current recorded in the absence of H_2O_2. The arrows indicate scan direction. The scans are offset by 1 mA cm^{-2}.

$4f_{5/2}$ peak. This confirms that little electrochemical oxidation of the UO_2 surface occurs at this potential. At the intermediate $[H_2O_2]$ the fraction of oxidized states, in particular the U^V state, in thesurface is significantly increased. The presence of U^V is confirmed by the development of the satellite peak at a binding energy 8.1 eV above the U $4f_{5/2}$ peak. At the higher $[H_2O_2]$, U^{VI} becomes the dominant oxidized state in the electrode surface as indicated by both the deconvolution of the two main peaks and the development of additional satellite peaks at binding energies of 4.0 eV and 10.0 eV above the U $4f_{5/2}$ peak consistent with the literature [48–50].

Fig. 12 shows the fractions of the individual oxidation states determined after the full range of potentiostatic experiments. While the exact amounts of individual oxidation states may be slightly suspect due to the inevitable difficulties involved in transferring electrodes from aqueous solution to the spectrometer vacuum chamber, our many previous studies have demonstrated that the trends are significant. In addition, since the analytical sampling depth is in the range of ~3 nm and the oxidized surface layer will be thinner than this, the fractions should be considered illustrative rather than quantitative. The increase in extent of oxi-

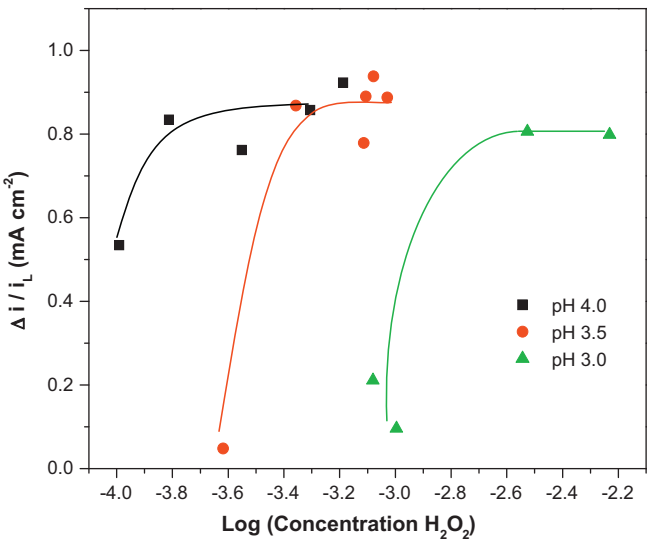

Fig. 9. The ratio of the background corrected currents (Δi) to the theoretical diffusion limiting current (i_L) as a function of $[H_2O_2]$ at −0.8 V in 0.1 mol L^{-1} NaCl solutions at $3 \leq pH \leq 4$. The lines in the figure are not fits to the data points.

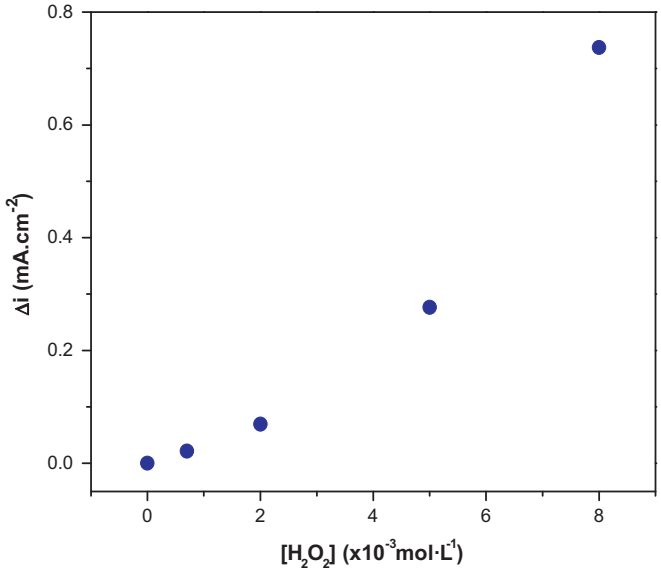

Fig. 10. Background corrected H_2O_2 reduction currents (Δi) as a function of $[H_2O_2]$ at pH 3.5 after applying a constant potential of −0.2 V for 1 h.

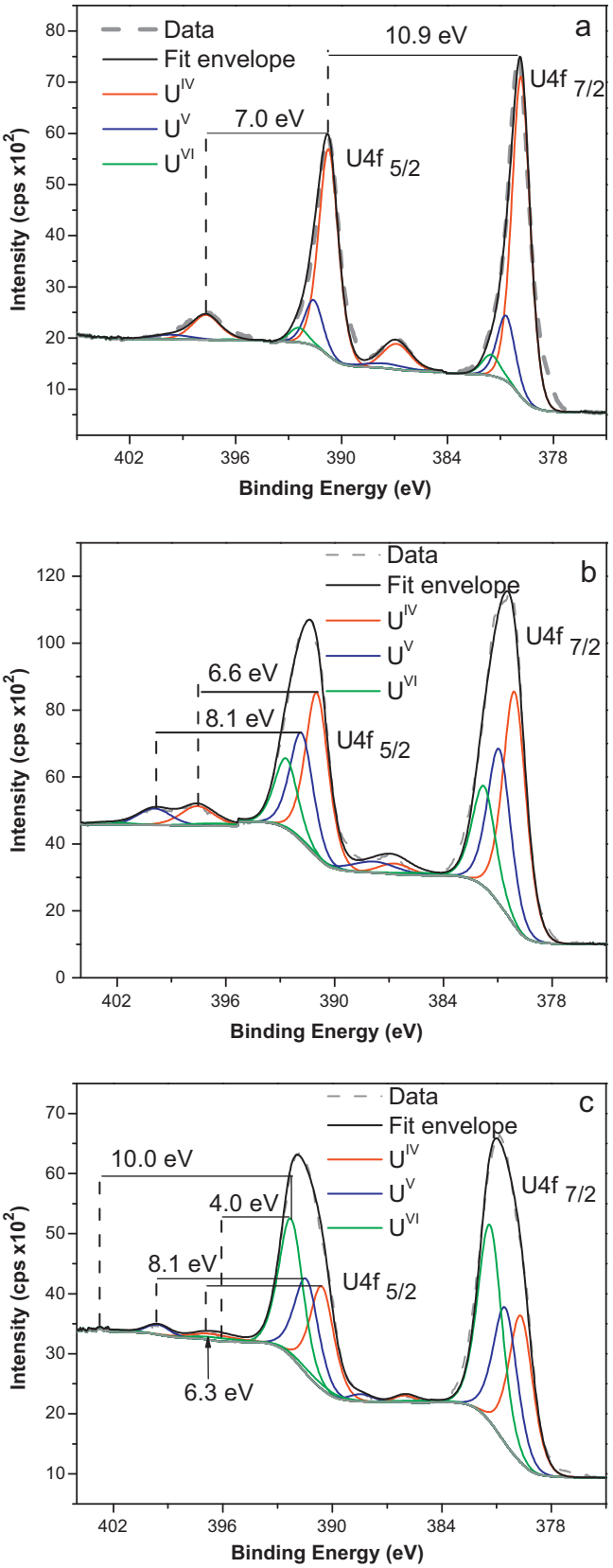

Fig. 11. Representative U 4f XPS spectra recorded on a 1.5 at.% SIMFUEL electrode in pH 3.5 solution under constant potential at −0.2 V for 1 h: (a) without H_2O_2 (b) with 2×10^{-3} mol L^{-1} and (c) 8×10^{-3} mol L^{-1} H_2O_2. The arrow indicates the separation between satellite and the U $4f_{5/2}$ peak.

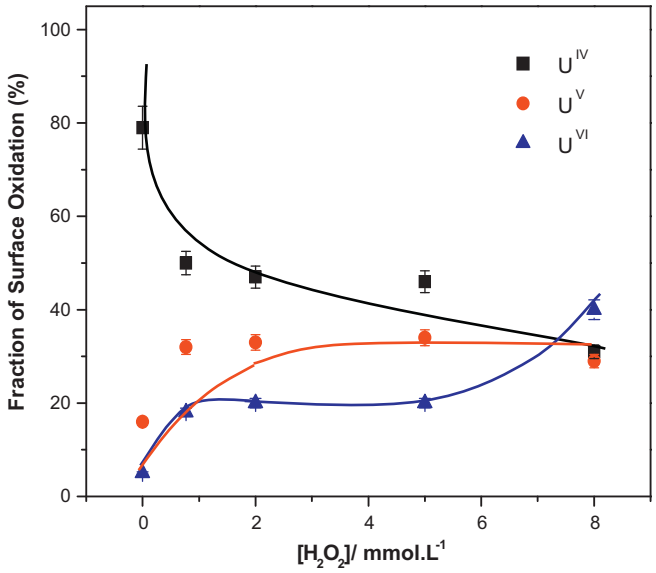

Fig. 12. Relative percentages of the three U oxidation states as a function $[H_2O_2]$ in 0.1 mol L^{-1} NaCl solutions at pH 3.5 at a potential of −0.2 V for 1 h.

dation of the electrode surface on adding H_2O_2 is consistent with the chemical oxidation of the surface to produce adsorbed oxidized states (reaction (2)). Additionally, the constant composition of the surface and the dominance of U^V over U^{VI} as the H_2O_2 reduction current increases (Fig. 9) can be attributed to the balance between the chemical production of the $(U^VO_2OH)_{ads}$ state, its catalysis of H_2O_2 reduction, and eventual destruction by either electrochemical reduction or further chemical oxidation to $(U^{VI}O_2(OH)_2)_{ads}$ and dissolution as soluble UO_2^{2+}. As noted above, the electrochemical oxidation of the chemically formed U^V intermediate should be minimal at −0.2 V [34]. The increased U^{VI} content of the surface at the highest $[H_2O_2]$ may indicate the increased rate of oxidation of $(U^VO_2OH)_{ads}$ to $(U^{VI}O_2(OH)_2)_{ads}$ by H_2O_2 prior to its dissolution.

3.3. Scanning electron microscopy (SEM)

Fig. 13 shows SEM micrographs of the freshly polished electrode surface and the electrode surface after the 1 h potentiostatic treatment in solutions containing 2×10^{-3} and 8×10^{-3} mol L^{-1} H_2O_2; i.e., at a low $[H_2O_2]/[H^+]$ ratio when acidic conditions will prevail at the electrode surface. The surface roughness shown in Fig. 12(a) is characteristic for a polished SIMFUEL electrode surface. After potentiostatic oxidation in the solution containing the low $[H_2O_2]$ there is no visible change in the morphology of the surface supporting the claim that at this concentration chemical dissolution is minimal and the chemical formation of $(U^VO_2OH)_{ads}$ is primarily balanced by its electrochemical reduction. At the higher concentration the electrode surface is considerably rougher and unevenly etched or pitted. This indicates that at this higher concentration the further oxidation/dissolution of the $(U^VO_2OH)_{ads}$ state occurs. The lateral variations in surface etching and pitting would be consistent with an uneven distribution of the oxidation/dissolution reaction which, at $[H_2O_2]/[H^+] \leq 1$, could lead to the coexistence of acidic and alkaline surface locations as suggested by the results in Figs. 2 and 6.

3.4. Summary

Fig. 14 attempts to illustrate schematically the mechanisms for H_2O_2 reduction operating in the two $[H_2O_2]/[H^+]$ regimes. If this ratio is ≥1, Fig. 14(a), then H_2O_2 reduction proceeds through the chemical formation of a $U^{IV}_{1-2x}U^V_{2x}O_{2+x}$ surface layer (1) in which

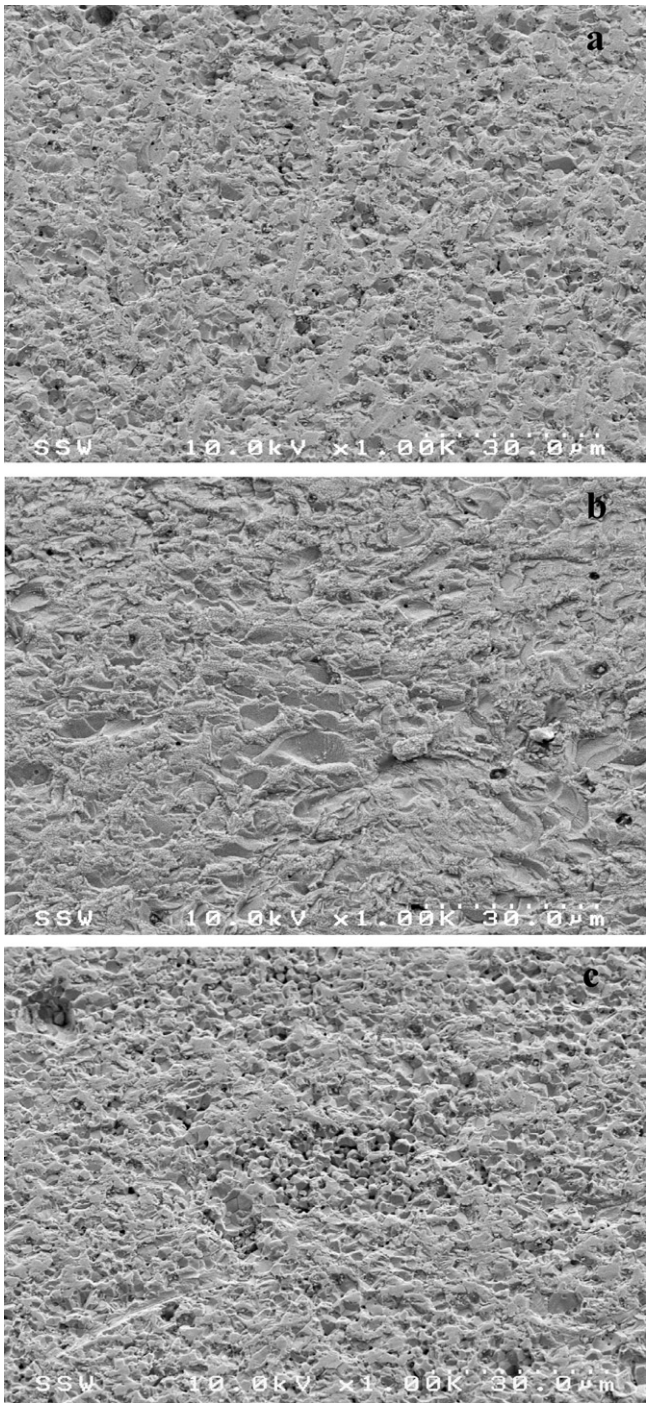

Fig. 13. SEM images collected at a magnification of 1000× on a 1.5 at.% SIMFUEL after a 1 h potentiostatic treatment in 0.1 mol L^{-1} NaCl solution at pH 3.5 containing $[H_2O_2]$ (a) freshly polished surface (b) 2×10^{-3} mol L^{-1} and (c) 8×10^{-3} mol L^{-1}.

O^{2-} anions are injected into the readily-available interstitial sites in the fluorite UO_2 lattice. Subsequently, this layer is reduced electrochemically (2) which involves the ejection of these O^{2-} anions (3). At the neutral to alkaline conditions prevailing at the electrode surface and the potentials required for the overall H_2O_2 reduction reaction to occur, the formation of U^{VI} species, which could lead to the oxidative dissolution of the UO_2, does not occur. Consequently, this layer is relatively stable and, for sufficiently high $[H_2O_2]$, the current for its reduction can approach the diffusion-controlled limit.

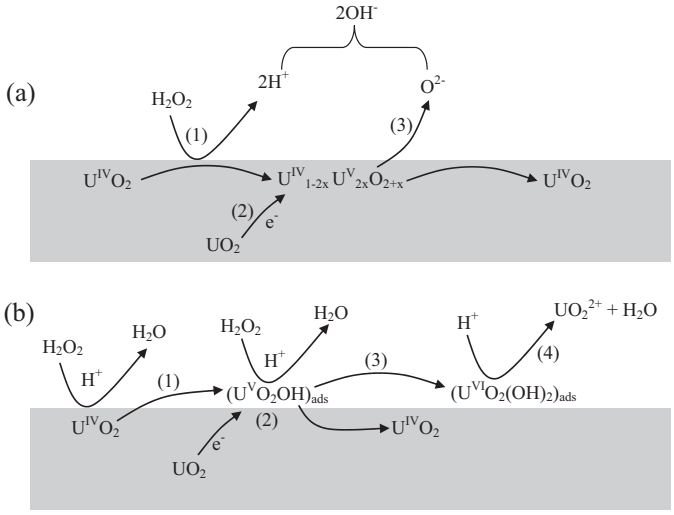

Fig. 14. Proposed mechanism for the reduction of H_2O_2 with UO_2 surfaces in acidic solutions (a) $[H_2O_2]/[H^+] \geq 1$ and (b) $[H_2O_2]/[H^+] < 1$.

When the $[H_2O_2]/[H^+]$ ratio is <1, Fig. 14(b), this $U^{IV}{}_{1-2x}U^{V}{}_{2x}O_{2+x}$ layer is not stable and H_2O_2 reduction proceeds via the chemical formation (1) and electrochemical reduction (2) of a $(U^{V}O_2OH)_{ads}$ surface intermediate. However, this intermediate can also be further chemically oxidized (3) and dissolved (4). This instability to both electrochemical reduction and chemical oxidation prevents the H_2O_2 reduction current from achieving the diffusion-controlled limit.

Acknowledgements

This research is funded under the Industrial Research Chair agreement between the Canadian Natural Sciences and Engineering Research Council (NSERC) and Nuclear Waste Management Organization (NWMO), Toronto, Canada. Surface Science Western is acknowledged for the use of their XPS and SEM equipment. The authors would also like to thank Dr. J. C. Wren for the use of her UV/vis spectrophotometer.

References

[1] J. McMurry, D.A. Dixon, J.D. Garroni, B.M. Ikeda, S. Stroes-Gascoyne, P. Baumgartner, T.W. Melnyk, Ontario Power Generation Report: 06819-REP-01200-10092-R00, 2003.
[2] Nuclear Waste Management Organization (NWMO), Choosing a way forward: the future management of Canada's used nuclear fuel. November 2005, http://www.nwmo.ca.
[3] D.W. Shoesmith, NWMO TR-2007-03, Nuclear Waste Management Organization, Toronto, Canada, 2007.
[4] S. Sunder, N.H. Miller, D.W. Shoesmith, Corrosion Science 46 (2004) 1095.
[5] D.W. Shoesmith, Journal of Nuclear Science and Technology 282 (2000) 1.
[6] J.S. Goldik, H.W. Nesbitt, J.J. Noël, D.W. Shoesmith, Electrochimica Acta 49 (2004) 1699.
[7] J.S. Goldik, J.J. Noël, D.W. Shoesmith, Journal of the Electrochemical Society 153 (2006) E151.
[8] J.S. Goldik, J.J. Noël, D.W. Shoesmith, Electrochimica Acta 51 (2006) 3278.
[9] J.S. Goldik, J.J. Noël, D.W. Shoesmith, Journal of Electroanalytical Chemistry 582 (2005) 241.
[10] B.G. Santos, J.J. Noël, D.W. Shoesmith, Journal of Electroanalytical Chemistry 586 (2006) 1.
[11] B.G. Santos, J.J. Noël, D.W. Shoesmith, Electrochimica Acta 51 (2006) 4157.
[12] P.G. Keech, J.J. Noël, D.W. Shoesmith, Electrochimica Acta 53 (2008) 5675.
[13] J.C. Wren, D.W. Shoesmith, S. Sunder, Journal of the Electrochemical Society 152 (2005) B470.
[14] D.W. Shoesmith, J.J. Noël, F. Garisto, Materials Research Society Symposium Proceedings 824 (2004) 81.
[15] W.J. Cheong, P.G. Keech, J.C. Wren, D.W. Shoesmith, Z. Qin, Materials Research Society Symposium Proceedings 985 (2007) 27.
[16] H. Christensen, R. Forsyth, L. Lundquist, L.O. Werme, Radiation induced dissolution of UO_2 Studsvik Report NS-90185, Studsvik Energiteknik AB, Nykoping, Sweden, 1990.

[17] M.E. Broczkowski, P.G. Keech, J.J. Noël, D.W. Shoesmith, Journal of the Electrochemical Society 157 (2010) C275.
[18] Olivia Roth, J.A. LaVerne, Journal of Physical Chemistry A 115 (2011) 700.
[19] J. De Pablo, I. Casasa, J. Gimenez, V. Marti, M.E. Torrero, Journal of Nuclear Materials 232 (1996) 138.
[20] C. Corbel, G. Sattonnay, S. Guilbert, F. Garrido, M.-F. Barthe, C. Jegou, Journal of Nuclear Materials 348 (2006) 1.
[21] M.J. Nicol, C.R.S. Needes, Electrochimica Acta 20 (1975) 585.
[22] I. Grenthe, J. Fuger, R.J. Konings, R.J. Lemire, A.B. Muller, C. Nguyen-Trung, H. Wanne, Chemical Thermodynamics of Uranium, North Holland, Amsterdam, 1992.
[23] M. Amme, B. Renker, B. Schmid, M.P. Feth, H. Bertagnolli, W. Dobelin, Journal of Nuclear Materials 306 (2002) 202.
[24] P. Diaz-Arocas, J. Quinones, C. Maffiotte, J. Serrano, J. Garcia, J.R. Almazan, J. Esteban, Materials Research Society Symposium Proceedings 353 (1995) 641.
[25] K.A. Kubatko, K.B. Helean, A. Navrotsky, P.C. Burns, Science 302 (2003) 1191.
[26] G. Sattonnay, C. Ardois, C. Corbel, J.F. Lucchini, M.F. Barthe, F. Garrido, D. Gosset, Journal of Nuclear Materials 288 (2001) 11.
[27] T.Z. Forbes, P. Horan, T. Devine, D. McInnis, P.C. Burns, American Mineralogist 96 (2011) 202.
[28] L.E. Eary, L.M. Cathles, Metallurgical Transactions B 14B (1983) 325.
[29] F. Clarens, J. De Pablo, I. Casas, J. Gimenez, M. Rovira, J. Merino, E. Cera, J. Bruno, J. Quinones, A. Martınez-Esparza, Journal of Nuclear Materials 345 (2005) 225.
[30] F. Clarens, J. De Pablo, I. Diez-Perez, I. Casas, J. Gimenez, M. Rovira, Environmental Science and Technology 38 (2004) 6656.
[31] B. Hanson, B. McNamara, E. Buck, J. Friese, E. Jenson, K. Krupka, B. Arey, Radiochima Acta 93 (2005) 159.
[32] A. Rey, S. Utsunomiya, J. Gimenez, I. Casas, J.D. Pablo, R.C. Ewing, American Mineralogist 94 (2009) 229.
[33] P.G. Lucuta, R.A. Verrall, H. Matzke, B.J. Palmer, Journal of Nuclear Materials 178 (1991) 48.
[34] B.G. Santos, H.W. Nesbitt, J.J. Noël, D.W. Shoesmith, Electrochimica Acta 49 (2004) 1863.
[35] C.J. Hochanadel, Journal of Physical Chemistry 56 (1952) 587.
[36] I. Stefanic, J.A. LaVerne, Journal of Physical Chemistry A 106 (2002) 447.
[37] G.C. Allen, N.R. Holmes, Journal of the Chemical Society, Dalton Transactions 12 (1987) 3009.
[38] E.S. Ilton, A. Haiduc, C.O. Moses, S.M. Heald, D.C. Eldbert, D.R. Veblen, Geochimica et Cosmochimica Acta 68 (2004) 2417.
[39] S. Sunder, G.D. Boyer, N.H. Miller, Journal of Nuclear Materials 175 (1990) 163.
[40] M. Schindler, F.C. Hawthorne, M.S. Freund, P.C. Burns, Geochimica et Cosmochimica Acta 73 (2009) 2488.
[41] E.S. Ilton, A. Haiduc, C.L. Cahil, A.R. Felmy, Inorganic Chemistry 44 (2005) 2986.
[42] E.S. Ilton, J.F. Boily, P.S. Bagus, Surface Science 601 (2007) 908.
[43] E.S. Ilton, P.S. Bagus, Surface and Interface Analysis 43 (2011) 1549.
[44] M.E. Broczkowski, J.J. Noël, D.W. Shoesmith, Journal of Nuclear Materials 346 (2005) 16.
[45] M.E. Broczkowski, R. Zhu, Z. Ding, J.J. Noël, D.W. Shoesmith, Materials Research Society Symposium Proceedings 932 (2006) 449.
[46] J. Paquette, R.J. Lemire, Nuclear Science and Engineering 79 (1981) 26.
[47] A.J. Bard, L.R. Faulkner, Electrochemical Methods, 2nd ed., Wiley, Toronto, 2001 (Chapter 9).
[48] Y.A. Teterin, V.M. Kulakov, A.S. Baev, N.B. Nevzorov, I.V. Melnikov, V.A. Streltsov, L.G. Mashirov, D.N. Suglobov, A.G. Zelenkov, Physics and Chemistry of Minerals 7 (1981) 151.
[49] S. Bera, S.K. Sali, S. Sampath, S.V. Narasimhan, V. Venugopal, Journal of Nuclear Materials 255 (1998) 26.
[50] S. Van den Berghe, J.-P. Laval, B. Gaudreau, H. Terryn, M. Verwerft, Journal of Nuclear Science and Technology 277 (2000) 28.
[51] E.S. Ilton, P.S. Bagus, Physical Review B: Condensed Matter 71 (2005) 195121.